Deuteron-deuteron elastic scattering at 231.8 MeV

A. M. Micherdzińska,[1] P. V. Pancella,[2] E. J. Stephenson,[1] A. D. Bacher,[1,3] C. E. Allgower,[1] A. C. Fonseca,[4] C. M. Lavelle,[1]
H. Nann,[1,3] J. Olmsted,[1] M. A. Pickar,[5] and A. Smith[6]

[1]*Indiana University Cyclotron Facility, Bloomington, Indiana 47408, USA*
[2]*Physics Department, Western Michigan University, Kalamazoo, Michigan 49008, USA*
[3]*Department of Physics, Indiana University, Bloomington, Indiana 47405, USA*
[4]*Centro de Física Nuclear, Universidade de Lisboa, 1649-003 Lisboa, Portugal*
[5]*Department of Physics and Astronomy, Minnesota State University-Mankato, Mankato, Minnesota 56001, USA*
[6]*Physics Department, Hillsdale College, Hillsdale, Michigan 49242, USA*
(Received 29 December 2006; published 9 May 2007)

We report angular distribution measurements of the differential cross section $\sigma(\theta)$ and the analyzing powers $iT_{11}(\theta)$, $T_{20}(\theta)$, and $T_{22}(\theta)$ for deuteron-deuteron elastic scattering at 231.8 MeV. These data are compared to calculations based on the lowest order terms in the Born series expansion of the Alt-Grassberger-Sandhas equation for four nucleons interacting through the CD Bonn potential.

I. INTRODUCTION

In 2003 we reported measurements of the total cross section for the charge symmetry breaking (CSB) $d + d \rightarrow {}^4\text{He} + \pi^0$ reaction at 228.5 and 231.8 MeV [1]. The small cross sections (12.7 ± 2.2 and 15.1 ± 3.1 pb, respectively) have received theoretical attention [2,3] because of the potential connection to CSB in the quark sector. There CSB arises from the down-up quark mass difference $m_d - m_u$ and electromagnetic effects [4–6].

An initial investigation of the processes that contribute to this reaction [2] included pion production directly from the nucleon, rescattering of such a pion, and production in association with the exchange of a heavy meson or photon. Estimates of each term made use of Gaussian bound state wave functions and plane wave two-body relative motion. Even so, the calculations for the total reaction cross section were comparable to the results of the CSB experiment.

A better estimate would require the use of more appropriate wave functions that include isospin mixing and a treatment of the interaction between the two deuterons in the initial state. An investigation along these lines has been reported by Nogga *et al.* [3] where it is found that the increased high-momentum components of the more realistic wave functions as well as the inclusion of initial state interactions increase the theoretical CSB total cross sections and tend to worsen agreement with the experiment. The initial state interactions in particular have a significant effect on the prediction; thus, the quality of this estimate is crucial to a proper understanding of the CSB reaction. The initial state interactions involved four-body dynamics in a region where calculations had not been made previously. Such calculations are summarized here.

At the time of the CSB experiment, it was recognized that it would be important to have a way to confirm the accuracy of the initial state interactions between the two incoming deuterons. So a part of the running time assigned to the CSB experiment was devoted to a measurement of the differential cross section $\sigma(\theta)$ and analyzing power $iT_{11}(\theta)$, $T_{20}(\theta)$, and $T_{22}(\theta)$ angular distributions for deuteron-deuteron elastic scattering

at 231.8 MeV, the larger of the two energies for the CSB experiment. Other measurements of $d + d$ elastic scattering exist, but the data are at too low an energy [7,8] or represent too small a collection of measurements [9] to be of use for evaluating these theoretical calculations.

Near pion production threshold, the outgoing pion channel is mainly S wave. Production of the pion can come only through the ${}^3\text{P}_0$ entrance channel partial wave because of parity and spin coupling constraints. Nevertheless, our expectation was that the spin dependence observed for elastic scattering along with the cross section would test the four-body calculation (summed over all partial waves), from which we might be able to infer the accuracy of the calculated ${}^3\text{P}_0$ partial wave.

The theoretical formalism used to describe the data is based on the solution of the Alt, Grassberger, and Sandhas (AGS) equations [10] for four strongly interacting nucleons. Because these equations are still very hard to solve at energies above four-body breakup threshold ($E_{\text{c.m.}} \geqslant 4.4$ MeV), we develop an approximation based on the lowest order terms in the Neumann series expansion of the AGS equations, which we expect to work at center of mass energies $E_{\text{c.m.}} \geqslant 100$ MeV and at smaller scattering angles where a single-scattering approximation is more nearly valid. In lowest order, this approximation to $d + d$ elastic scattering proceeds via the breakup of one of the deuterons in the initial state, intermediate three-nucleon scattering involving either one of the two separated nucleons and the second deuteron, and final recombination into a deuteron of the two nucleons. The scattering is described by a fully off-shell three-nucleon t-matrix. The comparison with data may reflect the quality of this lowest order approximation as well as the quality of the deuteron wave functions and the three-body t-matrix.

The experiment is detailed in Secs. II–V, which describe in turn the detector system, the measurements of the beam polarization, the $d + d$ elastic scattering analyzing powers, and the $d + d$ differential cross section. Sections VI and VII summarize the elastic scattering calculations and compare those calculations with the data.
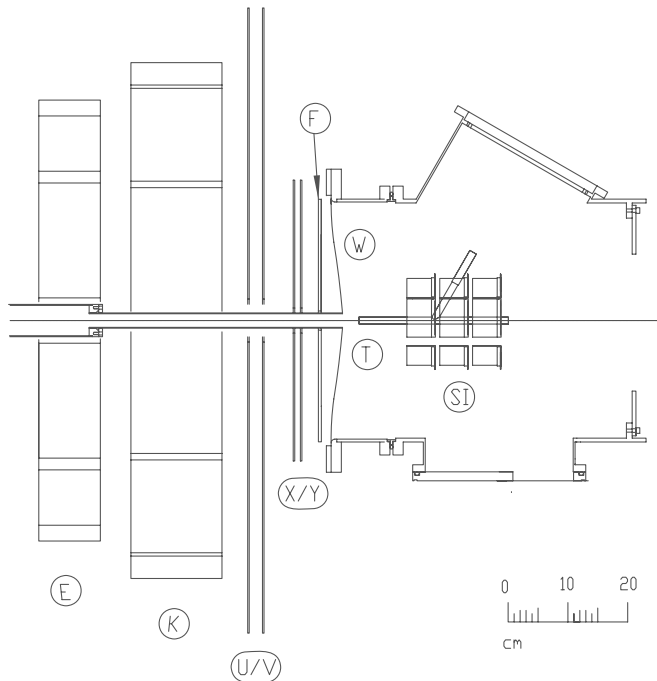
FIG. 1. A top view of the layout of the PINTEX detector system showing the target compression tube (T), the surrounding Si barrel array (SI), and the forward detector array that was mounted in air past the stainless-steel exit window (W). The beam traveled from right to left. The forward detectors consisted (in order) of the F thin plastic scintillator, the XY and UV wire chamber planes, and the two thick K and E plastic scintillators. During the experiment, the silicon barrel (see Fig. 2) was located further downstream than shown here so that it was centered on the target tube.

II. DETECTOR SYSTEM AND RUNNING PLAN

The measurements of the total cross section for the $d + d \rightarrow {}^4\mathrm{He} + \pi^0$ reaction were made with the electron-cooled synchrotron and storage ring (Cooler) at the Indiana University Cyclotron Facility (IUCF) [11]. That experiment was located in the section of the Cooler ring containing a 6° bend that we used to separate the forward-going ${}^4\mathrm{He}$ recoil nuclei from the circulating beam. In another straight section of the ring there was a general purpose detector system supported by the PINTEX collaboration [12]. At the completion of the CSB experiment in 2002, we kept the Cooler ring beam energy at 231.8 MeV and made the switch from the operation of the CSB apparatus to the PINTEX detector system. At the same time, we also changed to the injection of a polarized deuteron beam. This enabled us to continue with only a short interruption and make the elastic scattering measurements reported here.

The PINTEX target chamber and detector [13] shown in Fig. 1 had three main components: (1) the target compression tube, (2) the Si barrel array, and (3) the forward detector system consisting of a series of plastic scintillators and wire chambers. The target gas was contained within an open-ended, thin-walled (50 μm) aluminum tube 27.5 cm long and 1.2 cm in diameter. The inside of the tube was coated with Teflon because it also served in other experiments to contain polarized atoms. The wall of this tube was the only material through which recoil
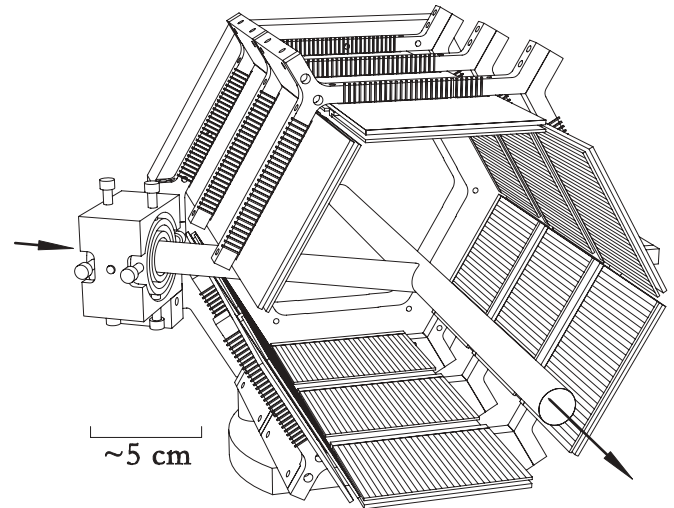

FIG. 2. Perspective view of the hexagonal Si barrel array and target tube. The silicon strip detectors were arranged along six sides with three detectors each and individual strips running parallel to the beam.

particles had to pass on their way to the silicon strip detector array. Target gas (unpolarized hydrogen or deuterium) was fed into this tube through a small Teflon hose (1 mm in diameter) attached to a fitting near the center. Gas flowed at low pressure into the middle of the target tube and out both ends where it dispersed and was pumped away.

The Si barrel array consisted of 18 silicon strip detectors arranged in a hexagonal structure with six rows of 3 detectors each as shown in Fig. 2. The 18 strips on each detector were oriented along the beam direction. This arrangement provided fine spacing in azimuthal angle for the purpose of checking the coplanarity for two-body final states. The 12 detectors located upstream had thicknesses of 1.0 mm while the 6 downstream detectors had thicknesses of 0.5 mm. Readout of the silicon strips consisted of individual preamplifiers and pulse shaping amplifiers. Discriminators recorded any strip with a signal above threshold for trigger logic and timing.

Particles going forward (see Fig. 1) exited the Cooler ring vacuum through a thin (0.18 mm) stainless steel window. The first scintillator, called the F detector, was 1.5 mm thick and divided in half horizontally. This detector measured dE/dx for charged particles, which was combined with signals from the thicker K and E scintillators downstream to provide particle identification. The K detector was divided into four quadrants and the E detector into eight octants, all optically isolated. The thicknesses of these two scintillator layers were 153 and 103 mm, respectively. A central hole in each scintillator assembly allowed for the passage of the vacuum pipe containing the circulating Cooler beam. For each scintillation detector, position information from the particle track was used to calculate a correction to the scintillator pulse height information for the light collection efficiency to obtain more uniform information on the deposited energy.

There were two sets of wire chambers (MWPCs) for particle tracking. Each set consisted of wires running in perpendicular directions separated by high voltage planes

made of aluminized Mylar. At the center of each chamber was a hole for the beam pipe. The central hub around the pipe was supported entirely by the sense wires and Mylar foils. The first chamber had wires running vertically and horizontally (Y and X planes). To aid in the elimination of multiple track ambiguities, the orientation of the second plane was rotated by $45°$ about the beam axis (U and V planes). The wire chamber readout consisted of a series of latching registers that were strobed by a signal from the scintillator trigger circuit.

The trigger for $d + d$ elastic scattering consisted of a coincidence between two properly oriented segments of the F and K detectors along with a hit on at least one strip of the Si barrel array. For the forward-going track, the scintillators provided particle identification and total energy and the wire chambers determined the spherical-coordinate angles θ and ϕ. For the recoil track, it was possible in most cases to confirm the particle type from the correlation between energy deposited in the silicon detector and the polar angle of the forward track. The specific Si strip localized the azimuthal angle of the recoil ϕ_r relative to the center axis of the target tube.

While this arrangement provided a way to observe $d + d$ elastic scattering events, we also needed a way to determine the polarization of the circulating deuteron beam and the absolute luminosity. Using the same beam, we changed to a hydrogen target because $d + p$ elastic scattering could serve as a reference reaction whose cross section and analyzing powers were known from other experiments. The details concerning how this information was used are covered in the next three sections.

The trigger for $d + p$ elastic scattering consisted of two forward particles striking opposite halves of the F and K detectors. In this case, energy and particle identification information was available for both particles in addition to full angle information, either (θ_p, ϕ_p) or (θ_d, ϕ_d). This is more kinematic information than was available for $d + d$ elastic scattering, and as a result it was possible to reconstruct the point of scatter within the target tube without additional information.

The deuteron beam for this experiment was generated by a pulsed atomic beam source [14]. Charge exchange with a negative atomic hydrogen beam produced polarized D⁻ ions for acceleration. Once extracted, these ions were accelerated to 4 MeV in a radiofrequency quadrupole. The beam pulse, which lasted up to $400\,\mu$s, was strip-injected into the Cooler injector synchrotron. There the beam was bunched into a narrow pulse, accelerated to 110 MeV, and transferred to the Cooler ring. The Cooler accumulated up to 15 bunches using electron cooling to merge them into the same phase space volume. The Cooler injector synchrotron was cycled at 0.8 Hz to produce the pulses for injection into the Cooler. Once the Cooler was filled with a current of roughly $100\,\mu$A, the Cooler ring was operated as a synchrotron to accelerate the beam to 231.8 MeV. After arriving at the final energy, target gas flow was turned on for typically about 100 s of data taking. Then the beam was dumped and the Cooler magnetic fields recycled in preparation for the next injection.

To follow any possible slow changes in the deuteron beam polarization, the target gas was changed from D_2 to H_2 for 2 h out of every 8 h during the experiment. Even so, it was

TABLE I. Ion source polarization states.

State	1st trans.	2nd trans.	p_y	p_{yy}
Unp	None	None	0	0
V+	MF $3 \to 4$	SF $2 \to 3$	1	1
V−	MF $1 \to 4$	WF $2 \to 4$	−1	1
T+	MF $1 \to 4$	SF $2 \to 6$	0	1
T−	MF $1 \to 4$	SF $3 \to 5$	0	−2

not possible to guarantee that the luminosity (product of beam current and target thickness) was the same for the two target gases. So two sets of runs were made at the beginning and end of the experiment using molecular HD gas. With identical luminosities for the hydrogen and deuterium components, we could extract the information needed to scale the $d + d$ elastic scattering cross sections to the $d + p$ reference. This analysis is discussed in Sec. V.

III. DEUTERON BEAM POLARIZATION MEASUREMENTS

The polarized deuteron beam was produced in an atomic beam source [14]. A general description of such sources may be found in a review article by Haeberli [15]. The source at IUCF had two polarizing stages, each of which consisted of a separator sextupole magnet followed by radio-frequency (RF) transition units. The first stage was accompanied by a medium-field unit; the second had two strong-field units and one weak-field unit. This arrangement permitted a variety of large vector (p_y) and tensor (p_{yy}) beam polarizations, where the polarizations are defined (with respect to the vertical $\hat{y}$ axis at the target) by $p_y = f_+ - f_-$ and $p_{yy} = 1 - 3f_0$, with f_+, f_0, and f_- being the fractions of the beam that are in the $m = 1$, 0, and −1 magnetic substates.

The five beam states used in this experiment are summarized in Table I. States V+ and V− have large and opposite vector polarizations and provide sensitivity to the vector analyzing power $iT_{11}(\theta)$. All of the polarization states have large tensor polarizations. By comparing the effects of states V+, V−, and T+ against state T−, we obtained information on the $T_{20}(\theta)$ and $T_{22}(\theta)$ tensor analyzing powers. Table I also contains the RF transition unit used in each stage of the polarized ion source (WF = weak field, MF = medium field, and SF = strong field) and the numbers of the hyperfine states involved in that particular transition, numbered 1 through 6 beginning with the state at the highest energy in a magnetic field (see Ref. [15]). If the separation sextupoles and RF transitions units had worked with perfect efficiency (and the beam was ionized in a very large magnetic field to avoid mixing among the hyperfine states) in a source without background, then the vector and tensor polarization for each state would assume the ideal values shown in Table I.

The polarization of each state from the ion source could be checked during beam setup by inserting a polarimeter into the beam line following the radiofrequency quadrupole accelerating section. This polarimeter consisted of a gas cell containing ^{3}He gas. Just ahead of the gas cell were four

TABLE II. Average beam polarizations.

State	Low energy		Cooler ring	
	p_y	p_{yy}	p_y	p_{yy}
V+	0.706 ± 0.049	0.832 ± 0.022	0.675 ± 0.020	0.790 ± 0.052
V−	-0.561 ± 0.049	0.602 ± 0.023	-0.617 ± 0.020	0.578 ± 0.051
T+	-0.033 ± 0.047	0.863 ± 0.022	0.000 ± 0.019	0.739 ± 0.053
T−	-0.121 ± 0.048	-1.558 ± 0.021	-0.001 ± 0.015	-1.852 ± 0.045

collimator jaws that were isolated so as to provide individual current readouts. This gave information used to center the beam passing through the gas cell and to confine the beam used for the measurement to a well-controlled geometry.

Protons from the $^3\text{He}(d, p)\,^4\text{He}$ reaction were observed by four plastic scintillation detectors. All of the detectors were in the horizontal plane, which was perpendicular to the vertical alignment of the beam polarization axis. The detectors were mounted to the left and right at laboratory angles of $67.5°$ and $135°$. A comparison of the count rates among these four detectors gave a value for the vector and tensor polarization of each of the polarization states, based on a calculated beam energy of 3.4 MeV at the center of the gas cell and analyzing powers from other experiments [16–18]. The average values for these "low energy" polarizations measured before and after the experiment are given in Table II. The errors quoted for the low energy measurements are statistical. In addition, the vector analyzing power for this polarimeter is small and the calibration scale uncertainty may be as large as 20%. These polarization measurements were used to adjust the operating parameters of the polarized ion source. The polarizations measured with the PINTEX apparatus in the Cooler ring are given in the two right-hand columns. We next turn to an explanation of how these values were obtained. All polarizations for the $d + d$ experiment were taken solely from the Cooler ring measurements.

Given an event set triggered on two forward tracks from a hydrogen target, we must identify the elastic scattering $d + p$ events and know which particle is which. Figure 3 shows the expected energy of the elastically scattered deuteron or proton as a function of its polar angle in the laboratory. If the angle of one of the two tracks was greater than $37°$, that track was assigned to the proton. Inside $37°$ (marked with a dashed vertical line), all of the proton energies are larger than the corresponding deuteron energies, which are marked by the heavy part of the deuteron kinematic locus in Fig. 3. So if neither of the two tracks had a polar angle greater than $37°$, the track with the largest energy was assigned to the proton.

Additional requirements were imposed on the data to make sure that the two-track events were in fact $d + p$ elastic scattering. Figure 4 shows the measured coplanarity, or the difference, $\phi_{12} = \phi_2 - \phi_1$, in azimuthal angle for the two forward tracks. The vertical dashed lines in Fig. 4 show the acceptance limits for our analysis ($\pm 10°$) on either side of $180°$.

Another requirement was placed on the sum of the energies of the two tracks, as shown in Fig. 5 for data with the coplanarity cut applied. All values between the dashed lines were retained in the analysis. As can be seen from the distribution of events, there are other processes contributing to energies below the elastic scattering peak near 231.8 MeV. These extra events, presumably from breakup, are not completely removed by this energy cut from the group of $d + p$ events. So a subtraction was made using scattering angle information, as is described next. (An investigation of the number of elastic $d + p$ events that lie below the
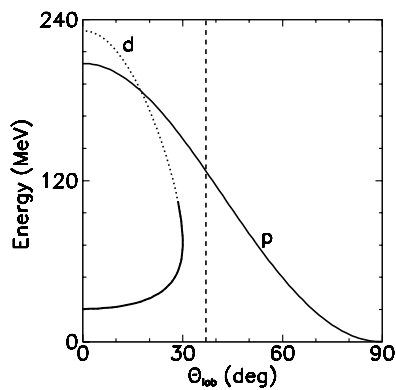

FIG. 3. Laboratory kinematic loci for $d + p$ elastic scattering at 231.8 MeV showing the energies for the deuteron and proton as a function of the laboratory polar angle θ. The heavy part of the deuteron locus shows the range of energies associated with proton angles less than $37°$ (vertical dashed line).
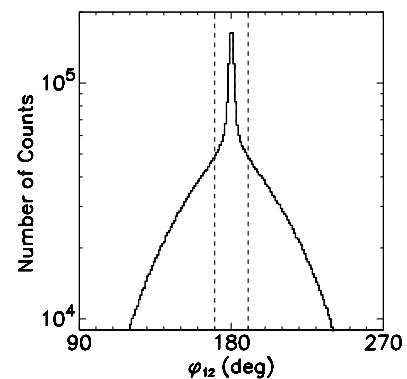

FIG. 4. Measurements of the coplanarity, $\phi_{12} = \phi_2 - \phi_1$, for two-track events in the forward detector. The dashed lines at $\pm 10°$ on either side of $180°$ indicate the acceptance limits chosen for the $d + p$ analysis. All events with a valid trigger and sufficient wire chamber information for analysis are included here.
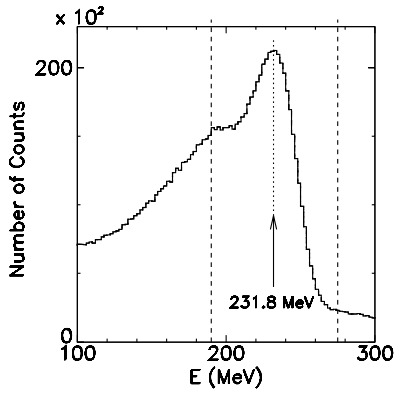
FIG. 5. Measurements of the total energy for the two-track events. The dashed lines represent the acceptance limits for this sum. These events fall inside the acceptance limits in coplanarity, as shown in Fig. 4.

lower cut is discussed in Sec. V along with the cross section measurements.)

One additional requirement on $d + p$ elastic scattering events is that the polar angles for the deuteron and proton follow the kinematic locus for elastic scattering. This relationship is shown by the intense distribution of events in Fig. 6. The solid line marks the expected relationship between deuteron and proton laboratory polar angles. The events well separated from this locus belong to other processes. Edges in the plot at $37°$ for both θ_p and θ_d arise from the selection scheme used to assign tracks as either a deuteron or a proton. (The locus disappears below $\theta_p \sim 20°$ because the protons did not cross the trigger threshold in the F detector.)

One way to obtain a one-dimensional representation of these data to quantify background subtraction is to refer the angle to the kinematic locus. The difference between the measured and kinematically calculated deuteron angle is given by $D \equiv \theta_{d,\text{data}} - \theta_{d,\text{kin}}$. For events within some chosen range of proton angles, a graph of D can be used to establish the level of the background and provide a sample of such background events. A distribution of D is shown in Fig. 7 with cuts applied for coplanarity and total energy. Background
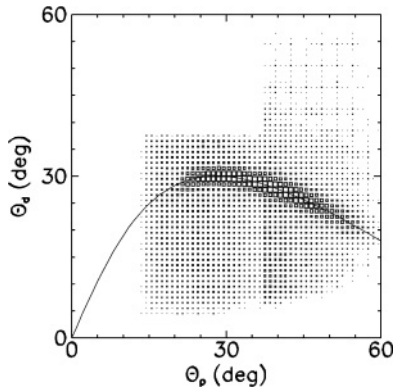

FIG. 6. The distribution of events against deuteron and proton polar laboratory angles. The ridge represents $d + p$ elastic scattering. The kinematic relationship expected for elastic scattering is shown by the solid curve.
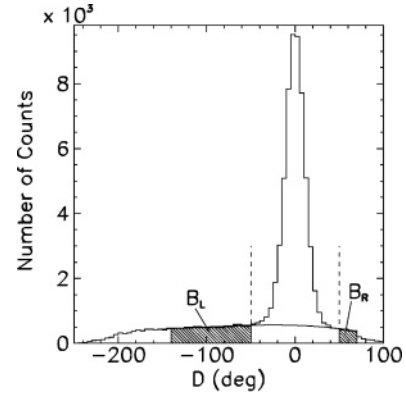

FIG. 7. Measurements of the difference function $D \equiv \phi_{d,\text{data}} - \phi_{d,\text{kin}}$ for the proton laboratory angle range from $23.9°$ to $51.1°$ and polarization state T$-$. Two background regions are shown by the hashed areas and labeled B_L and B_R. A polynomial fit to the spectrum in these background regions is shown by the solid curve. The dashed lines are the acceptance limits for good $d + p$ events.

regions B_L and B_R on either side of the peak at $D = 0$ were used to define a low-order polynomial that was assumed to represent the shape of the background throughout the region. As is described below, the polarization was obtained from the distribution of events as a function of the azimuthal angle ϕ. The events that were selected for this calculation came from the region of the plot of D that lies between the two background-defining regions or dashed lines. This selection included some background events. The number of those events was given by the area under the smooth polynomial curve within this region. The ϕ dependence of the background was taken from the events in the two background regions. Before the polarizations were calculated, the background ϕ distribution was subtracted from the ϕ distribution containing the good $d+p$ events after scaling that background distribution so that its total number of events matched the area under the background curve in the region of the good $d + p$ events.

From the laboratory polar angles, the center-of-mass scattering angles were calculated using the usual kinematic relationships. The $d + p$ events were divided into bins $2.5°$ wide in the center-of-mass angle. The subtraction described above was made for each center-of-mass angle bin using a fit to the background shape for data within that bin.

Samples of the ϕ distributions for the five polarization states are summed over the range from $\theta_{\text{c.m.}} = 75°$ to $130°$ ($\theta_{\text{lab}} = 23.9°$ to $51.1°$) and shown in Fig. 8. Notches are clearly visible every $90°$ where there is an aligned gap in the segmented detectors. These notches distort the shape of the ϕ distribution and make it difficult to observe the polarization effects that should appear as simple cosine shapes on top of a zero offset for each case. To remove this efficiency effect, we divided each of the polarized state ϕ distributions by the unpolarized ϕ distribution. The results are shown in Fig. 9. These ϕ distributions show smooth oscillations that contain the desired polarization information.

To model the ϕ dependence, it is most appropriate to quote the polarized cross section using spherical tensor notation. However, we would also like to include the simplicity of the
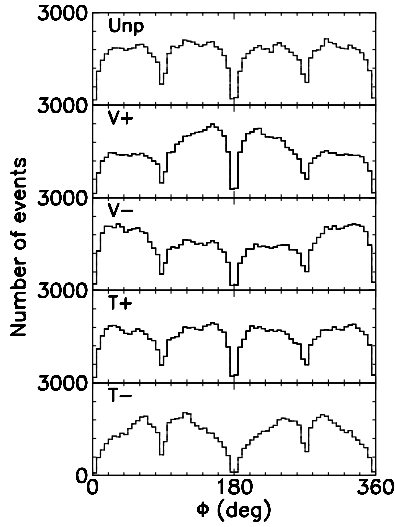
FIG. 8. Measured distributions of $d + p$ elastic scattering events against the azimuthal angle ϕ for each of the five polarization states.

two polarization values, p_y and p_{yy}, which are in Cartesian notation. Using a mixed mode expression, we write the polarized cross section as

$$\sigma(\theta, \phi) = \sigma_{\text{unp}}(\theta)\left(1 + \sqrt{3}p_y i T_{11}(\theta)\cos\phi - p_{yy}\right.$$
$$\left.\times\left[\frac{1}{\sqrt{8}}T_{20}(\theta) + \frac{\sqrt{3}}{2}T_{22}(\theta)\cos 2\phi\right]\right). \quad (1)$$

Following the ϕ dependence in this expression, the ϕ distributions for any polarization state shown in Fig. 9 can be represented by the function

$$C(\phi) = F + G\cos\phi + H\cos 2\phi. \quad (2)$$

For each of the background-subtracted ϕ distributions from $d + p$ elastic scattering, the coefficients F, G, and H were obtained using a least-squares minimization procedure. With
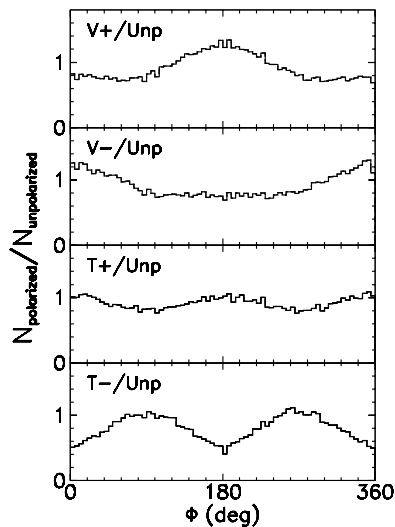

FIG. 9. ϕ distributions like those in Fig. 8 except that each polarized distribution has been divided by the unpolarized distribution.

reference to Eq. (1), we can express each of these coefficients as

$$F = C_0\left(1 - \frac{1}{\sqrt{8}}T_{20}(\theta)p_{yy}\right) \quad (3)$$

$$G = \sqrt{3}C_0 i T_{11}(\theta)p_y \quad (4)$$

$$H = -\frac{\sqrt{3}}{2}C_0 T_{22}(\theta)p_{yy}, \quad (5)$$

where C_0 is a single normalization coefficient that may be different for each ϕ distribution (a function of θ angle bin and polarization state). These three equations contain only three unknowns, C_0, p_y, and p_{yy}; so they can be solved to yield these quantities. Thus we can obtain a value of the beam polarization for each polarization state separately. It is assumed in this analysis scheme that the "unpolarized" state, which is produced by turning off the power to all ion source RF transition units, is unpolarized to a high degree since the ionization of the atomic beam occurs in a magnetic field that is a factor of several above the critical field [15]. This assumption may not have been fulfilled, and we will return to this question again at the end of this section.

The analyzing powers for each scattering angle bin were obtained by interpolating in angle and energy the measurements reported by Sekiguchi *et al.* [19] at 200 and 270 MeV. The first estimate of the analyzing powers at 231.8 MeV was made using a simple linear interpolation in energy between 200- and 270-MeV data points at the same scattering angle. This estimate was refined by using Faddeev three-body calculations [20] of $d + p$ elastic scattering made over the same range of energies, but in finer steps. For each center-of-mass angle, the values of the calculated analyzing power as a function of energy were reproduced by a polynomial. The difference at 231.8 MeV between that polynomial and a straight line through the calculated values at 200 and 270 MeV was added to the original linear interpolation from the data of Sekiguchi *et al.* [19]. In all cases these corrections were less than ±0.014.

This analysis yielded values of the polarization for every polarized beam state, every center-of-mass angle bin, and every H_2 target gas run. Simple consistency checks are shown in Figs. 10 and 11 by combining the data for all H_2 target runs together or for all angles together. In Fig. 10, the flatness of the data as a function of angle is a confirmation within the errors shown that the angular distributions of the analyzing powers extracted from the Sekiguchi data are accurate in angular shape. The flatness of Fig. 11 as a function of run number shows that the polarization was constant with time during the experiment. The data are shown separately for each polarization state. There are only two states shown for p_y, as the T+ and T− states were consistent with zero. The p_{yy} values for the V+ and T+ states in Figs. 10 and 11 have been displaced to either side of the center of the bin to make it easier to follow the size of the individual error bars. The average values for the polarization in each state are given in Table II.

The results in Table II raise additional issues concerning the quality of the polarization measurements. First, all of the tensor polarization values in Table II from the Cooler ring are shifted negatively when compared to the values taken at low
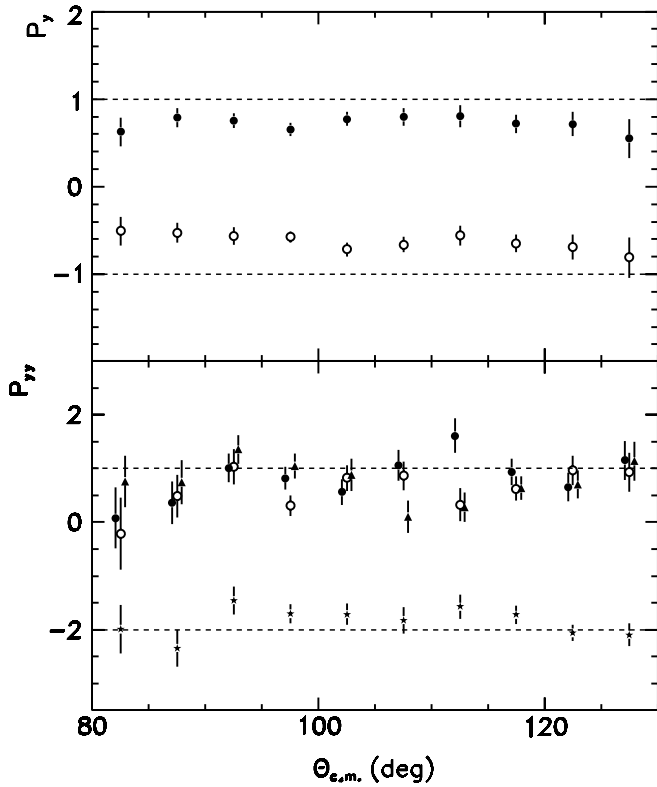
FIG. 10. Measurements of the beam polarization for each polarization state as a function of the center-of-mass $d+p$ scattering angle. The plotting symbols denote polarization states as solid = V+, open = V−, triangle = T+, and star = T−. Vector p_y polarizations for the T+ and T− states are consistent with zero and not plotted. These data are shown in 5° bins. The points are located at the center of the bin except for the V+ and T+ states for p_{yy} to better distinguish the errors for each measurement. The dashed lines indicate the physical limits for the polarization values. All $d+p$ runs are averaged together for each measurement. The errors are statistical only.
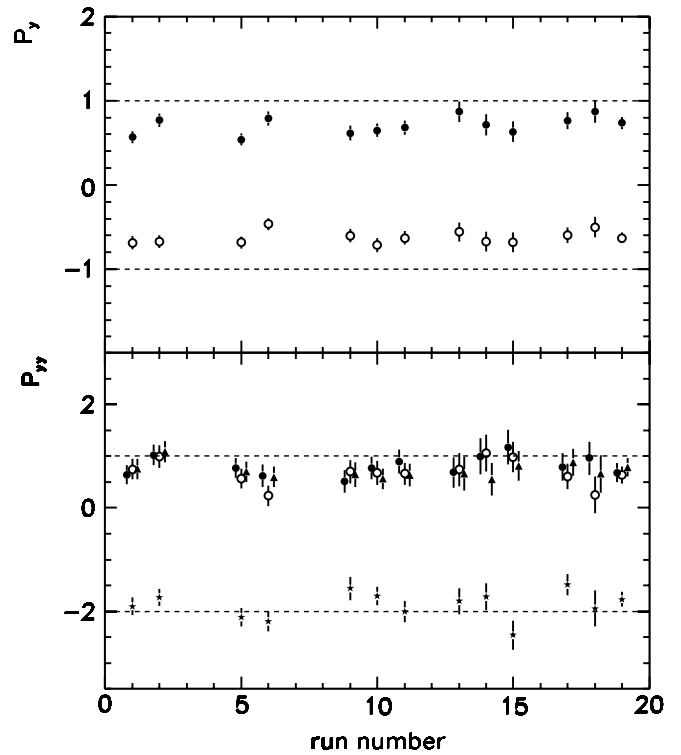

FIG. 11. Measurements similar to those in Fig. 10 except as a function of run number (time) during the experiment. Center-of-mass angles between 75° and 130° are averaged together for each point. The errors are statistical only.

energy, so that the V+, V−, and T+ states are less polarized while the T− state becomes more polarized. Values of the tensor polarizations taken during an earlier commissioning run using $d+p$ scattering do not show such a shift. One possible explanation is that the unpolarized state retained some residual polarization during the CSB experiment. This component would be introduced into the analysis by the division of each polarized ϕ distribution by the nominally unpolarized ϕ distribution. Since the low energy polarimeter measurements closely resemble the results from the earlier commissioning run, whatever mechanism may have produced this effect did not operate when the low energy measurements were made at the start and end of this experimental run. This is possible because a different ion source control sequence was used for low energy and Cooler operation.

During the earlier commissioning run, we found that the tensor polarizations measured using $d+p$ scattering with the Cooler ring were larger than those measured at low energy by about 7%. To untangle these two problems for this set of data, we extracted the size of the negative shift by requiring that the ratio of the tensor polarization in any of the V+, V−, or T+ states to the tensor polarization in the T− state be the same

between the low energy and the Cooler ring measurements. This requirement can be met with only the shift as a free parameter. Its average value over the V+, V−, and T+ states is $\Delta p_{yy} = -0.14$. If this shift had varied during the course of the experiment, values of the tensor polarizations would rise and fall together. A search for cross correlations between the tensor polarizations from the different states shown in Fig. 11 yielded no significant correlation. We conclude that the shift was present for all Cooler runs at the same level, regardless of whether the target was deuterium or hydrogen.

When this negative shift is removed from the Cooler tensor polarization values, then they are all larger than the values for the same state measured at low energy. The average ratio of Cooler to low energy tensor polarization is about 1.10, a change that could result from an error in the analyzing powers used as a reference in either case. There is no other evidence to indicate which, if either, of the low energy or Cooler polarizations is correct. For the purpose of this elastic scattering experiment, we will use the polarizations obtained at the energy of the Cooler ring. Within the precision of the measurements, we cannot detect any shift or rescaling of the vector polarization values between the low energy and Cooler polarization measurements.

If the interpretation of the tensor polarization shift is correct, it is an effect for both the measurement of the $d+d$ analyzing powers as well as the polarizations. Because the size of the shift is proportional to the tensor analyzing power, the effect of this systematic error will cancel when the division
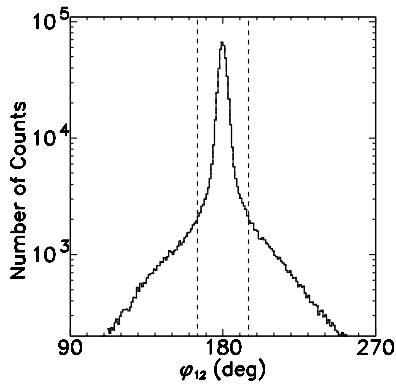
FIG. 12. Measurements of the coplanarity, $\phi_{12} \equiv \phi_2 - \phi_1$, for all events with a coincidence between a forward detector track and a hit in the Si barrel array. The dashed lines at $\pm 15°$ on either side of $180°$ are the acceptance limits for the $d + d$ analysis.

of the ϕ distribution by the unpolarized state data is made. Indeed, comparisons of the analyzing powers calculated from each polarization state (see Sec. IV) agree internally within statistical errors. This would not be the case if the shift were removed from the measured polarizations and the tensor analyzing powers recalculated with the unshifted values. This is additional evidence that the problem originates with a residual polarization in the unpolarized state. So we used the polarizations recorded in Table II for the $d + d$ analysis and did not attempt any further corrections to our $d + d$ data.

If the unpolarized state is indeed tensor polarized to some extent, then the unpolarized cross sections obtained from these data will not be correct. We incorporate this effect into the systematic error analysis for the cross sections, as described in Sec. V.

IV. D+D ELASTIC SCATTERING ANALYZING POWERS

For the $d + d$ elastic scattering events, we have less kinematic information available from the detectors. The events consist of one track in the forward scintillator detectors in coincidence with a signal from at least one of the silicon strip detectors. In addition to energy information for the forward track, position information is available from the wire chambers. This provides scattering angles (θ and ϕ) from the difference in the hit positions in the two wire chambers. For most of the angle range in $d + d$ elastic scattering, the recoil deuterons have enough energy to pass through the silicon detectors without stopping. So the silicon provides only a pulse height signal that may be correlated with other kinematic information. Thus the total $d + d$ energy is not available. The identification of a particular strip on the silicon detector gives a range of azimuthal angles equal to the strip width relative to the size of the beam in the target tube. Because of the orientation of the silicon detector strips and the extension of the target region along the beam, there is no useful information on the polar angle of the recoil particle.

It was possible to make a useful selection of events based on the requirement of coplanarity, as shown in Fig. 12. For $d + d$ scattering the acceptance limits are set farther apart than
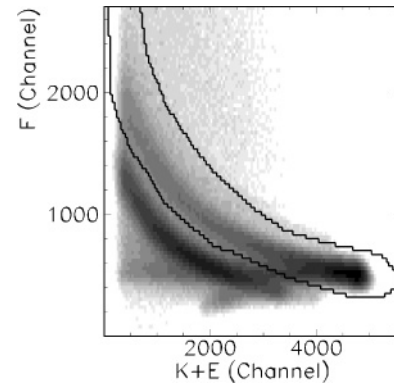

FIG. 13. The distribution of events in the forward detector as a function of the pulse height in the F detector and the sum of the pulse heights in the K and E detectors. The events shown are selected for coplanarity (Fig. 12) and silicon-detector particle identification (Fig. 14). The solid line indicates the acceptance limits in the analysis for events identified as deuterons.

for $d + p$, $\pm 15°$ about $180°$, because of smearing from the width (typically about $3°$) of the silicon detector strips.

For most of the candidate events, both particles could be identified with $d + d$ scattering. For the forward track, this identification was based on pulse height (dE/dx) in the F detector when compared against the sum of the energies deposited in the K and E detectors, as shown in Fig. 13. (The events populating Fig. 13 were selected to satisfy the coplanarity condition in Fig. 12 and the particle identification condition in Fig. 14.) The closed curve represents the acceptance limit for deuteron events.

For recoil particles, Fig. 14 shows a representative sample of events where the energy deposited in a 1.0-mm-thick silicon detector is plotted against the forward scattering angle. (The events shown in Fig. 14 were selected to satisfy the coplanarity condition in Fig. 12, the particle identification condition in
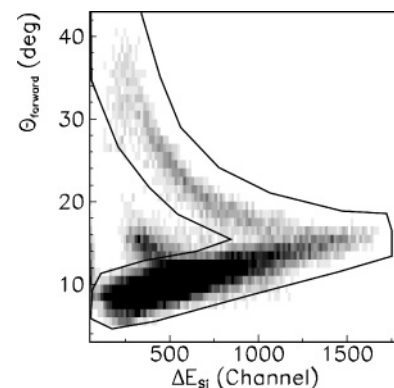

FIG. 14. The distribution of events as a function of polar angle θ of the forward track and the pulse height in a silicon detector. The events shown are selected for coplanarity (Fig. 12), forward detector particle identification (Fig. 13), and energy above the lower limit in Fig. 15. The solid line indicates the acceptance limits in the analysis for events identified as $d + d$ elastic scattering. Note the overlap with the proton locus from quasi-free $d + p$ scattering at forward track angles below $14°$.

Fig. 13, and the lower limit on forward detector energy shown in Fig. 15.) Because the energy of the recoil deuteron rises with rising forward scattering angle, this angle variable serves the same role as the dE/dx vertical scale in Fig. 13. Again, the solid curve represents the boundary of the acceptable deuteron events. At smaller silicon detector energies, a proton locus appears that is likely to be associated with quasi-free $d + p$ scattering. At the smaller forward scattering angles ($<14°$), this proton locus merges into the deuteron locus, and these two particles are not distinguishable. Throughout this region, there are protons from breakup events that will fall within the acceptance limits for deuterons.

The only correlation not yet used to select $d + d$ events is that between the energy and the scattering angle for the forward particle. We examined the energy distribution in a series of scattering angle bins. Figure 15 shows the ratio of the measured energy to that expected from a kinematic calculation. The example shown is for $\theta_{c.m.} = 21.5°$ and the unpolarized state. The largest peak is $d + d$ elastic scattering. Other processes are not well separated from the elastic scattering and generate more features and a long tail extending to lower energies. Just as in the $d + p$ case, we must find a way to subtract any background from the ϕ distribution data that will be used to determine the analyzing powers. What appears to be an extra unresolved peak just below the $d + d$ elastic peak also appears when we examine data taken with a hydrogen target and require the trigger and analysis selection criteria used for the $d + d$ analysis. We conclude that this feature is associated with $d + p$ quasi-elastic scattering. This peak appears most prominently at smaller deuteron angles because of our inability to distinguish recoil deuterons from protons in the silicon detectors (as shown in Fig. 14). These background events will have to be removed from the data sample before we can calculate the $d + d$ observables. Assuming that the spin dependence of $d + p$ elastic scattering closely resembles that for $d + p$ quasi-elastic scattering from the $d + d$ system, and assuming that other breakup channels are not important close to the $d + d$ elastic scattering peak, we can use the hydrogen target data to provide our sample of background events. We allowed the normalization of this background component to vary with scattering angle to account for the influence of the extra neutron in the four-nucleon system.

At larger scattering angles, the peak associated with quasi-elastic scattering fades away, in part because the recoil protons fall outside the silicon detector particle identification cut shown in Fig. 14. Another smooth component from breakup remains. We parametrized this by the function $(a_1 + a_2 E)/\{1 + \exp[(E - E_0)/a_3]\}$, where a_1, a_2, a_3, and E_0 were adjustable parameters. In Fig. 15, this component provides the smooth tail below the quasi-elastic background peak for $E_{det}/E_{kin} < 0.85$. The final shape of the background with both quasi-elastic and breakup contributions is shown as the dark-hashed area, and the difference that we assign to $d + d$ elastic scattering as the light-hashed area.

In most angle bins (above $E_{det}/E_{kin} = 0.6$ in Fig. 15), a significant low energy tail remains after the background subtraction. For the spin observables, these events were simply rejected by a sharp cut in energy, as shown by the dashed line in the Fig. 15 example. Presumably, some of them
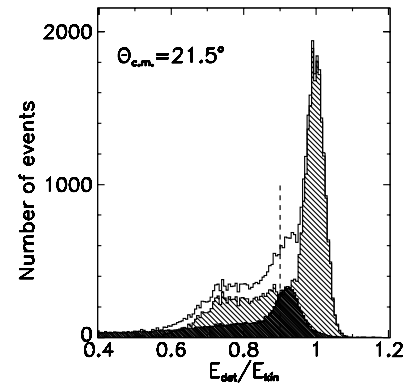

FIG. 15. Spectrum for the energy of the forward track at $21.5°$ divided by the energy expected from kinematics. The data shown here have passed the acceptance cuts shown in Figs. 12–14. The dark-hashed region is a background composed of the sum of a smoothly parametrized piece and a scaled quasi-elastic peak taken from hydrogen target data. The difference is shown by the light-hashed region. The lower acceptance limit for the $d + d$ analysis is shown by the vertical dashed line.

represent final state recoil particles that really have less energy, originating in processess that are not elastic scattering, while an unknown fraction may be valid elastically scattered deuterons whose energy was not fully captured. Their positions are not correlated with joints between scintillator detector elements, a point to which we return when considering corrections to the cross section. Cutting such events should not affect the $d + d$ spin observables. The data that were retained for the ϕ distribution analysis all lay above the acceptance cut noted by the vertical dashed line in Fig. 15. The final result of using this model was to obtain a coefficient to place in front of the ϕ distribution obtained from the hydrogen data before subtracting it from the $d + d$ data.

Examples of the ϕ distributions for $d + d$ elastic scattering are shown in Fig. 16. This illustration contains all of the data between center-of-mass angles of $10°$ and $89°$. Compared to the $d + p$ results shown in Fig. 8, these results are considerably more ragged. In addition to the scintillator gaps that occur every $90°$, there are gaps every $60°$ in the silicon barrel array with alternating wide and narrow widths. In addition, one detector in the upstream ring of six failed to record any events, leaving a hole at large values of ϕ in this plot. As we did with the $d + p$ analysis, we will assume that these inefficiencies are spin independent. Division of the polarized ϕ distribution by the unpolarized distribution is able to recover smooth ϕ distributions usable for analysis, as shown in Fig. 17.

We are again in a position where we can reproduce these normalized ϕ distributions of Fig. 17 using the coefficients of Eq. (2). This yields Eqs. (3)–(5), but now there are three unknown analyzing powers rather than two unknown polarizations. Without further information, a solution is not possible. To recover a set of solvable equations, we chose to rescale the unpolarized ϕ distribution by the relative luminosities between the polarized and unpolarized states. This sets the factor of C_0 to a value of one, leaving
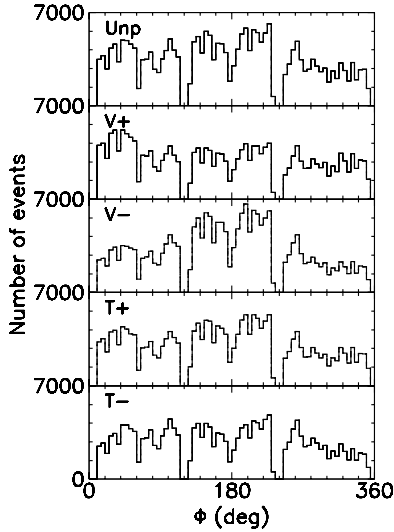
FIG. 16. Measurements of the dependence on the azimuthal angle ϕ of $d + d$ elastic scattering events for each of the five polarization states. The origin of the notches and other inefficiencies is discussed in the text.

(for each θ bin)

$$iT_{11}(\theta) = \frac{1}{\sqrt{3}}\frac{G(\theta)}{p_y} \qquad (6)$$

$$T_{20}(\theta) = \sqrt{8}\frac{1 - F(\theta)}{p_{yy}} \qquad (7)$$

$$T_{22}(\theta) = -\frac{2}{\sqrt{3}}\frac{H(\theta)}{p_{yy}}. \qquad (8)$$

We used the total trigger rate for two forward tracks as a spin-independent measure of the relative luminosities. The spin independence was checked against a continuous readout of the beam current transformer located near the PINTEX detector during times when the gas feed pressure was stable.

As discussed in the previous section, the unpolarized state may have retained some residual polarization so that the Cooler values in Table II are not the real beam polarizations. Instead, they are effectively the difference between the polarizations in the "polarized" and "unpolarized" states. This difference is multiplied by the relevant analyzing power, whether for $d + p$ or $d + d$, to obtain the asymmetries that drive the changes to the observed ϕ dependence. By using the Cooler polarization values in Table II as they are, we cancel the effects of this error for the calculation of the $d + d$ analyzing powers because the altered polarization cancels from the expression for the analyzing powers. Finally, we are simply scaling our results to the analyzing power reference values from Sekiguchi *et al.* [19]. The confirmation that this procedure works is that the analyzing powers measured with different polarization states agree (except for a statistical issue regarding T_{20} to which we now turn).

A lack of such consistency among polarization states appeared for $T_{20}(\theta)$ when the analyzing power values from the V+, V−, and T+ states were more positive at larger angles than the values from the T− states. This could arise from values of $F(\theta)$ that were systematically too low when
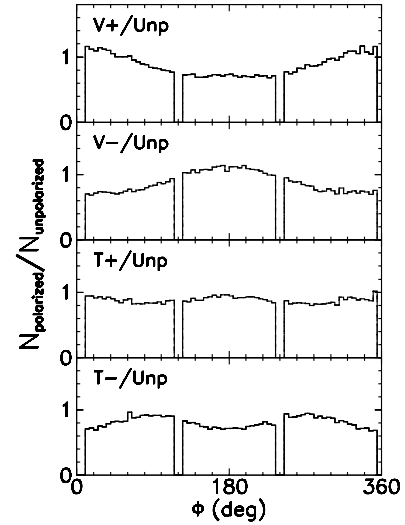

FIG. 17. Measurements of the dependence on the azimuthal angle ϕ of $d + d$ elastic scattering events for each of the four polarization states divided by the unpolarized state. The three remaining notches reflect gaps in the silicon detector array that are wider than the bins in this plot.

the $d + d$ cross section was small (at the larger scattering angles). In such cases, the $d + d$ peak was also relatively small compared to the background. This problem was traced to the division by the unpolarized ϕ distribution. Since this quantity enters into the denominator of the ratio shown in Fig. 17, its contribution to the errors on each data point was not symmetric, resulting in errors that were different on the two sides of the ratios. This creates a bias in the least-squares minimization routine that extracts the values of F, G, and H [see Eq. (2)] because the routine determines relative weights from a single value for the error. We suppressed this problem by reducing the number of bins in the ϕ distribution and fitting the total and background ϕ distributions separately. The increased number of events in each bin made the statistical errors smaller and more symmetric. Each result was carried through to an analyzing power. A weighted subtraction was made using the relative weight for the background contribution to the total peak sum. This produced consistent analyzing powers for all of the polarization states.

The extracted analyzing powers for $d + d$ elastic scattering at 231.8 MeV are shown in Figs. 18–20. The values of these observables are not very large. A detailed comparison with theory (solid curves) is presented in Sec. VII.

V. CROSS SECTION MEASUREMENTS

Cross section measurements with the Cooler ring are difficult because there is no *direct* source of information about the luminosity, the product of the number of particles passing through the target tube per unit time and the areal density of the gas in the tube at the location of the beam. One way to address this is to simultaneously monitor some process whose cross section is known while observing the reaction of interest. In the case of a deuteron beam and deuterium target at 231.8 MeV,
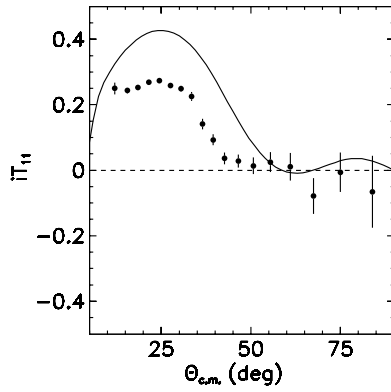
FIG. 18. Angular distribution measurements of the analyzing power $iT_{11}(\theta)$. The errors are statistical only. The comparison to the theoretical curve (solid line) is discussed in Sec. VII.

there are no processes with known cross sections. One must be introduced by adding another material into the deuterium gas. We chose to add hydrogen and to use $d + p$ elastic scattering as the reference cross section because measurements are available in this energy range (equivalent to proton beam kinetic energy $E_p = 116$ MeV in reverse kinematics) from published experiments. The comparison for the cross section normalization can be made if the target gas is molecular HD, because this forces the luminosities for $d + d$ and $d + p$ elastic scattering to be identical. With both types of event trigger running simultaneously, one can compare the number of elastic events for each case. Corrections must be applied for any detector efficiency or solid angle acceptance differences between the two event streams. Finally, the procedure for the data analysis must be investigated to determine what remaining systematic errors apply to the normalization of the final data.

For the reference cross section, we chose the recent measurements of Ermisch *et al.* [21] from the KVI. These data were measured across the full angular range and at six proton energies between 108 and 190 MeV. These data agree to within ±15% with older measurements in this same energy range [22–26]. A potential problem is that the KVI measurements lie about 30% above data at 135 MeV proton energy from RIKEN [19]. Because of this difference, the Japanese have recently remeasured this data at both RIKEN and RCNP, finding agreement with their previous values [27].
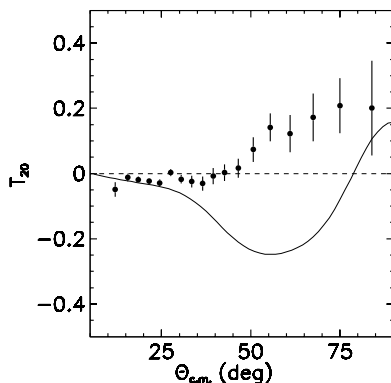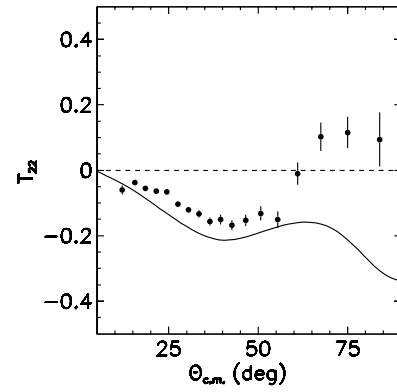

FIG. 19. Same as Fig. 18 except for T_{20}.

FIG. 20. Same as Fig. 18 except for T_{22}.

Until this problem is resolved, we cannot be certain that the reference cross sections for this work will not change downward, rescaling our data down by the same amount. Either the KVI data should be reevaluated or a third-party measurement is needed.

As is clear from the discussion in the two previous sections, both the $d + d$ and $d + p$ data sets have significant background to subtract even after all analysis cuts are applied. With the HD target, this situation becomes more complicated because both the hydrogen and deuterium components introduce extra events into the acceptance cuts for the opposite scattering process. Rather than deal directly with the background subtraction issue, we used an alternate scheme in which the only information extracted from the HD target run was the relative luminosity for all of the D_2 data compared with all of the H_2 data. This permits us to avoid making any background subtraction here and dealing with the problems that would be created by our choice of a subtraction method.

For whatever event selection scheme is used, the spectra in the HD runs will be the sum of similar spectra from the H_2 and D_2 runs with coefficients A and B as

$$[HD] = A[H_2] + B[D_2] \qquad (9)$$

where the brackets refer to any sum or spectrum of events that fall within a given acceptance, provided that same sum or spectrum and acceptance is used for all bracketed quantities in the equation. The coefficients A and B are the ratios of the integrated luminosity in the HD runs to the integrated luminosities in the H_2 and D_2 runs, respectively. To eliminate polarization effects, only data taken with the (nominally) unpolarized beam are included. By using the $d + p$ and $d + d$ triggers and cuts, we chose a subset of all events that emphasized the elastic scattering from either the H_2 or D_2 targets. No background subtractions were made for the data from any of the three target gasses. By choosing an even sample that emphasized each type of elastic scattering, this scheme provided two independent equations that can be solved for the coefficients A and B as shown in matrix form by

$$\begin{bmatrix} [HD]_{d+d} \\ [HD]_{d+p} \end{bmatrix} = \begin{bmatrix} [H_2]_{d+d} & [D_2]_{d+d} \\ [H_2]_{d+p} & [D_2]_{d+p} \end{bmatrix} \begin{bmatrix} A \\ B \end{bmatrix}, \qquad (10)$$
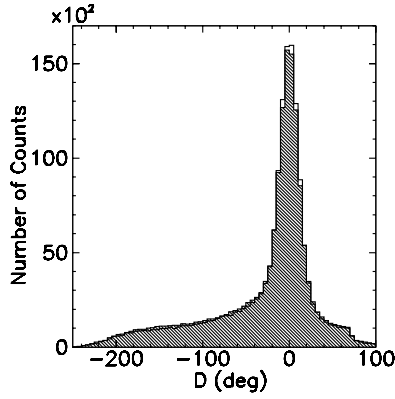
FIG. 21. Measurements of the angle difference for $d + p$ elastic scattering as shown previously in Fig. 7. The unfilled histogram comes from the HD data and the hashed histogram from the sum of the unpolarized part of the H_2 and D_2 runs with the coefficients A and B. Note the significantly larger background as compared to Fig. 7.

where the subscripts denote the analysis cuts. This scheme was completed for the data in this experiment with the result that $A = 1.035$ and $B = 0.513$ with negligable statistical errors. Even though relatively little beam time was devoted to running with the HD target gas, all of that running was unpolarized. A check of the validity of this analysis is shown in Figs. 21 and 22, which compare representative spectra from the HD target with the same spectra from the H_2 and D_2 runs. The relative normalization makes use of the A and B coefficients. Figure 21 shows a slightly more narrow $d + p$ peak for the HD gas than for the sum of H_2 and D_2 gas runs. Otherwise, there is excellent overlap between the two spectra in each case, thus supporting the values obtained for the two coefficients.

With the relative sizes of A and B, we can calculate the $d + d$ cross section in a given angle bin $\theta_{c.m.}$ by using the expression

$$\sigma_{d+d}(\theta_{c.m.}) = \left\langle \frac{\sigma_{d+p} \, \Omega_{d+p}}{N_{d+p}} \right\rangle \frac{B}{A} \frac{\epsilon_{d+p}}{\epsilon_{d+d}(\theta_{c.m.})} \frac{N_{d+d}(\theta_{c.m.})}{\Omega_{d+d}(\theta_{c.m.})},$$
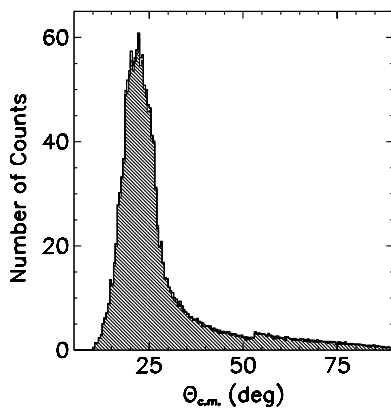
(11)

FIG. 22. Measurements of the forward deuteron angle for $d + d$ elastic scattering events. This figure follows the conventions of Fig. 21.
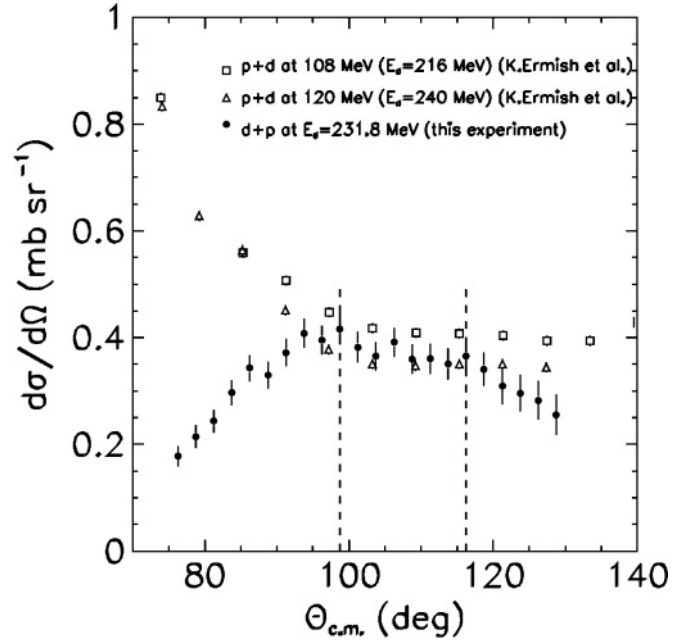

FIG. 23. Our measurements (solid) of the number of events per angle bin in the $d + p$ data divided by the solid angle and efficiency, and normalized to the measured $d + p$ cross sections from the experiment of Ermisch, represented by the squares ($E_p = 108$ MeV) and triangles ($E_p = 120$ MeV).

where N is the number of unpolarized events recorded in a particular angle bin, Ω is the solid angle, and ϵ is the efficiency for recording data. The three $d + p$ quantities in brackets are averaged over a range of $\theta_{c.m.} = 97.5°$ to $117.5°$ where we find that the efficiency for $d + p$ events is large and smooth enough that these data may be compared directly with the Ermisch data from the KVI [21]. That efficiency is given by ϵ_{d+p}.

The KVI measurements as a function of energy and angle were reproduced by a polynomial. Our measurements were normalized to this curve in the region between the two dashed lines in Fig. 23. This figure compares the $d + p$ angular distribution from this run, after normalization, with the Ermisch data at two neighboring energies. The efficiency at the larger center-of-mass angles goes down because the increasing forward proton energies produced signals in the F detector that were below the hardware threshold. At smaller angles, the proton laboratory angle increases and protons from different parts of the target pass outside the acceptance of the forward scintillation K detector.

The remaining task is to evaluate all of the efficiency factors for both the $d + p$ and $d + d$ analyses and to incorporate those factors into the equation for the $d + d$ cross section. This evaluation also provides an opportunity to note any factors that carry a significant systematic error (with or without a correction factor) so that this error can be included when considering the comparison with theory. These corrections to the cross section are given in Table III as inefficiencies (amount of data lost). We summarize each entry in order.

For $d + p$ events, the wire chambers provide eight pieces of information (x, y, u, and v for two tracks). Reconstruction can take place even if one of the eight pieces is missing. From

TABLE III. Inefficiencies and systematic errors (θ dependence quoted as a range).

Cause	Inefficiency (%)		Uncertainty (%)
	$d + p$	$d + d$	
Wire chambers	1.4	0.0	
Coplanarity cut	0.2	0.0	
Track chi square	5.9		
Forward PID		1	
Silicon PID		3	
Energy cut/tail	21		0 to +56
ϕ notches	13.5	27	±13
Forward detector			±10 (to −37)
Missing silicon θ		36 to 69	
Residual polarization			±1.7

the number of occurrences of losing one out of eight, it was possible to calculate the chance that more than one piece of information was gone and reconstruction was aborted by the software.

The regions outside the coplanarity cuts shown in Figs. 4 and 12 were examined for two-body events. Essentially none were found.

In the $d + p$ case, tracks whose wire chamber hits produced a poor reconstruction were discarded. This inefficiency was evaluated for events in the peak of the angle difference function shown in Fig. 7 and found to be 5.9%.

In the $d + d$ case, we estimated the number of events excluded using the particle identification (PID) cuts shown in Figs. 13 and 14 by counting the extra events that appeared when these cuts were enlarged. In a similar fashion, the silicon particle identification was also checked for losses.

The largest inefficiency for $d + p$ events came from the lower cut on total energy shown in Fig. 5. A low energy tail on the total energy could arise from incomplete light collection in the scintillator, a problem that can come from nuclear reactions in the scintillator or passage of the particle out of the active volume. As the lower acceptance cut in Fig. 5 is moved to lower pulse heights, more $d + p$ events are retained by the rest of the system. This allows us to estimate the inefficiency produced by the cut. But the background increases more rapidly than the number of useful events, so lower acceptance cuts do not improve precision.

Perhaps the most serious issue for the $d + d$ cross section is the decision to exclude the tail shown in Fig. 15 from the peak sum. If this tail had been systematically included, cross sections would have risen by as much as 56% at the most forward angles. Despite the regular appearance of a tail on all peaks, this feature increased as a fraction of the peak itself at the forward angles where the discrimination between protons and deuterons no longer existed in the silicon detectors. For this reason, this change was included as a systematic error rather than a correction.

Figure 8 shows that the efficiency is clearly reduced for certain ranges of ϕ associated with boundaries in the plastic scintillators. Using unpolarized data, we estimated the

inefficiency by simply assuming that a count rate at a level corresponding to the average of the highest channels in the ϕ distribution corresponded to complete efficiency. There does not appear to be any correlation between events which were lost because they passed through the cracks in scintillator coverage (notches in Fig. 8) and events that were lost because of a low recorded energy. This would favor reactions in the scintillator as the primary reason for low energy tails leading to incomplete light collection and event loss from the final data set. Such a tail is evident as the horizontal band below F detector channel 600 in Fig. 13. Events whose tracks passed into the notches between the scintillator elements did not produce triggers. So the energy tail and ϕ notch loss mechanisms were treated as independent and the corrections were added.

For the $d + d$ case, the ϕ distribution for unpolarized beam is shown in the top panel of Fig. 16. This distribution is considerably more ragged than its $d + p$ counterpart in Fig. 8. In addition to the notches produced every 90° by the gaps in the scintillator array, there is another series of notches every 60° that comes from the gaps between the silicon detectors. These gaps are alternately small and large, so every 120° there is a major gap in which the events per bin go to zero. Between 240° and 300° there was a silicon detector in the most upstream ring that was not functioning. Even with these problems considered, there is no obvious area where one could say that the response is maximally efficient. We chose to average the higher channels between 0° and 240°, but this is subject to a significant uncertainty that we note in Table III. The inefficiency recorded from this graph in Table III is the lost area beneath this average value.

The silicon barrel array also has gaps in scattering angle θ as well as ϕ, and these do not have a signature in any spectrum. For estimating this correction to $d + d$ scattering, we required a Monte Carlo simulation of the acceptance. The calculation used a triangular distribution of events along the center axis of the target tube with its apex at the junction with the fill tube. Particles were tracked in the forward detector and the silicon barrel. Energy loss and multiple scattering variations in that loss were included. Additional random spread in the energy signals was introduced to account for variations in the energy readout from the silicon and scintillation detectors. Thresholds in this readout were set at values taken from representative spectra in the analysis.

To verify that the Monte Carlo model of the forward detector was satisfactory, we also calculated the acceptance as a function of $\theta_{c.m.}$ for $d + p$ events. For this simulation, the threshold in the F detector and the maximum angle in the K detector were particularly important. These parameters were tuned to match two spectra, the distribution along the beam direction of the scattering point inside the target tube and the distribution of scattering angles shown in Fig. 23. The measured Ermisch $d + p$ cross section was used in the event generator.

The Monte Carlo calculation was repeated for $d + d$ scattering. The silicon barrel array was added but without any gaps in ϕ to avoid double counting this inefficiency. This Monte Carlo model produced inefficiencies as a function of the angle of the forward deuteron. This range is indicated in
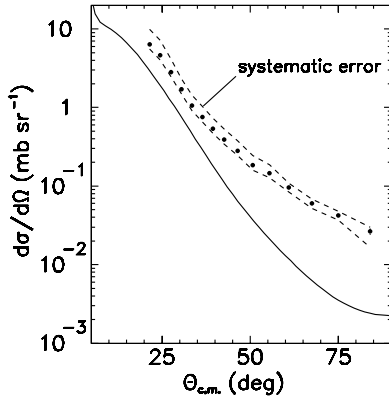
FIG. 24. Angular distribution of the $d + d$ differential cross section. The dashed lines outside the cross section measurements indicate the range of systematic error, both plus and minus, at that angle. The theoretical curve is discussed in Sec. VII.

Table III. Forward of the $\theta_{c.m.} = 21.5°$ bin, the efficiency fell sharply due to the action of thresholds in the silicon detectors. Rather than make a large and uncertain correction at the more forward angles, we chose to discard these data from the cross section angular distribution. The systematic error from the Monte Carlo calculation was taken to be ±10% except for angles sensitive to the two parameters tuned to match $d + p$ spectra.

The change in the cross section for either $d + p$ or $d + d$ elastic scattering due to the presence of a residual polarization in the unpolarized state can be estimated from the size of the T_{20} term in Eq. (1). For this estimate we took the $d + p$ analyzing power from our interpolation in Sec. III and the $d + d$ analyzing power from Fig. 19. Using a residual polarization of $p_{yy} = 0.14$ and combining the contributions from $d + p$ and $d + d$, we obtained the estimate of ±1.7% for the effect on the cross section analysis. Compared to other systematic errors, this effect is small.

The final values for the cross section angular distribution are shown in Fig. 24. We have included an upper and lower systematic error, which is indicated by the dashed lines above and below the measurements. Those errors are composed of contributions cited in Table III. It should be noted that the downward renormalization suggested by the recent Japanese measurements of the $d + p$ elastic scattering cross section was not included here, either as a correction or a systematic error. Further discussion of the comparison with theory (solid curve) is found in Sec. VII.

VI. FOUR-BODY SCATTERING FORMALISM

As mentioned in the Introduction, despite the tremendous progress achieved in recent years on the solution of the four-nucleon problem [28–31], most calculations are limited to energies below the four-particle breakup threshold (4.4 MeV). Nevertheless an understanding of nuclear reaction data involving two deuterons in the initial or final state at center of mass energies $E_{c.m.} > 100$ MeV requires developing initial or final state rescattering corrections that go beyond

the distortions obtained through an effective optical model potential fitted to the elastic $\vec{d} + d$ scattering data. At very high energies $E_{c.m.} > 500$ MeV the use of the Glauber approximation may be justified. Closer to pion production threshold where the wavelength associated with the relative $d + d$ on-shell momentum is of the order of 2.7 fm, i.e., close to the size of the deuteron, we find ourselves compelled to search for an approximate solution of the Yakubovsky [32] equation for the four-particle scattering wave function. Likewise, in $d + d$ elastic scattering at the same energies, there is a corresponding approximation of the AGS equations for the four-particle t-matrix that we test here as a means to verify the quality of the four-body calculation.

In the present work we develop an approximation based on the lowest order terms in the Born series expansion of the four-particle Yakubovsky equation. One starts from the original equation

$$
\left| \Psi_i^{\rho,\rho_0} \right\rangle = \delta_{\rho\rho_0} \left| \phi_i^{\rho_0} \right\rangle + \sum_j G_0 t_i G_0 U_{ij}^\rho \sum_\sigma \bar{\delta}_{\sigma\rho} \left| \Psi_j^{\sigma,\rho_0} \right\rangle, \quad (12)
$$

for the 18 components where ρ denotes one of the seven two-body partitions, four of $(3) + 1$ type, and three of $(2) + (2)$ type, and i denotes a pair interaction that is internal to ρ; j is both internal to σ and ρ. As usual, ρ_0 specifies the two-body entrance channel, $\bar{\delta}_{\sigma\rho} = 1 - \delta_{\sigma\rho}$, G_0 is the four free particle Green's function, t_i is the t matrix for pair i, and U_{ij}^ρ is the three-body t-matrix if ρ is of $(3) + 1$ type or the two noninteracting pair t matrix if ρ is of $(2) + (2)$ type. The initial state wave function component $|\phi_i^{\rho_0}\rangle$ carries the appropriate bound state wave function components of the target and/or projectile times a relative plane wave between their respective centers of mass. From Eq. (12) we construct the Neumann series expansion

$$
\left| \Psi_i^{\rho,\rho_0} \right\rangle \approx \delta_{\rho\rho_0} \left| \phi_i^{\rho_0} \right\rangle + \sum_j G_0 t_i G_0 U_{ij}^\rho \bar{\delta}_{\rho\rho_0} \left| \phi_j^{\rho_0} \right\rangle
$$
$$
+ \sum_{\beta kj} G_0 t_i G_0 U_{ik}^\rho G_0 t_k G_0 \bar{\delta}_{\rho\beta}
$$
$$
\times U_{kj}^\beta \bar{\delta}_{\beta\rho_0} \left| \phi_j^{\rho_0} \right\rangle + \dots. \quad (13)
$$

If the energy is sufficiently high one may retain only the first two terms, which already contain all orders of iteration in the pair interaction but first order in the three-body or pair-pair correlations.

If the initial state ρ_0 is a $(2) + (2)$ state then ρ, in the second term of Eq. (13), can only be a $(3) + 1$ two-body partition, because different $(2) + (2)$ partitions cannot share the same pair interaction that is internal to both of them. Therefore, in lowest order approximation and ρ_0 a $(2) + (2)$ state, one only needs to solve the three-body AGS equations for the operator U_{ij}^ρ, instead of the full Yakubovsky equation.

From the solution of the following three-body equation

$$
U_{ij}^\rho = \bar{\delta}_{ij} G_0^{-1} + \sum_k \bar{\delta}_{ik} t_k G_0 U_{kj}^\rho, \quad (14)
$$

where

$$t_k = v_k + v_u G_0 t_k, \qquad (15)$$

is the Lippmann-Schwinger equation for the k pair t-matrix, one gets

$$
\begin{aligned}
|\Psi^{\rho_0}\rangle &= \sum_{i\rho} |\Psi_i^{\rho,\rho_0}\rangle \approx |\phi^{\rho_0}\rangle \\
&\quad + \sum_j \sum_{i\rho} G_0 t_i G_0 U_{ij}^\rho \bar{\delta}_{\rho\rho_0} \left| \phi_j^{\rho_0} \right\rangle.
\end{aligned} \qquad (16)
$$

If we now look for the corresponding approximation for the four-particle AGS transition matrix $\mathcal{U}_{ij}^{\sigma\rho}$ that satisfies

$$
\begin{aligned}
\mathcal{U}_{ij}^{\sigma\rho} &= (G_0 t_i G_0)^{-1} \bar{\delta}_{\sigma\rho} \delta_{ij} \\
&\quad + \sum_{\alpha k} \bar{\delta}_{\sigma\alpha} U_{ik}^\alpha G_0 t_k G_0 \mathcal{U}_{kj}^{\alpha\rho},
\end{aligned} \qquad (17)
$$

we get

$$
\mathcal{U}_{ij}^{\sigma\rho} \approx (G_0 t_i G_0)^{-1} \bar{\delta}_{\sigma\rho} \delta_{ij} + \sum_\alpha \bar{\delta}_{\sigma\alpha} U_{ij}^\alpha \bar{\delta}_{\alpha\rho}, \qquad (18)
$$

from which one calculates all four-nucleon scattering amplitudes. If ρ and σ are $(2) + (2)$ channels, the first term is zero for the reasons mentioned above, and the $\rho \to \sigma$ transition amplitude

$$
\begin{aligned}
T^{\sigma\rho} &= \sum_{ij} \langle \phi_i^\sigma | \mathcal{U}_{ij}^{\sigma\rho} | \phi_j^\rho \rangle \\
&\approx \sum_{ij} \sum_\alpha \bar{\delta}_{\sigma\alpha} \left\langle \phi_i^\sigma U_{ij}^\alpha \phi_j^\rho \right\rangle \bar{\delta}_{\alpha\rho},
\end{aligned} \qquad (19)
$$

where α runs only over three-body $(3) + 1$ partitions much like in Eq. (16).

For four identical nucleons and two identical deuterons in the initial and final state, the $d + d$ elastic amplitude may be depicted as in Fig. 25. In lowest order, $d + d$ elastic scattering proceeds via deuteron breakup, intermediate nucleon-deuteron scattering, and final deuteron recombination. The fully off-shell $N + d$ elastic t-matrix U is integrated over the momentum of the fourth particle and folded on two deuteron wave
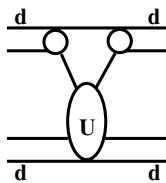

FIG. 25. Deuteron-deuteron elastic scattering amplitude where U is the nucleon-deuteron t-matrix.

functions that pertain to the initial and final state, respectively,

$$
\begin{aligned}
&\langle \mathbf{k}_0', \nu_1', \nu_2' | T(E) | \mathbf{k}_0, \nu_1, \nu_2 \rangle \\
&= \int d^3 k \left\langle \phi_d \left(\frac{1}{2}\mathbf{k}_0' - \mathbf{k}; \nu_1' \right) \right| \\
&\quad \times \left\langle \mathbf{k}_0' - \frac{2}{3}\mathbf{k}; \nu_2' \right| (1 + P_{12}') \\
&\quad \times U \left(E - \frac{4}{3}k^2 \right) (1 + P_{12}') \left| \mathbf{k}_0 - \frac{2}{3}\mathbf{k}; \nu_2 \right\rangle \\
&\quad \times \left| \phi_d \left(\frac{1}{2}\mathbf{k}_0 - \mathbf{k}; \nu_1 \right) \right\rangle,
\end{aligned} \qquad (20)
$$

where the parameters ν denote discrete quantum numbers in the initial and final states and $P_{12}(P_{12}')$ is a permutation operator for the two deuterons in the initial (final) state. The three-body t-matrix U is the properly symmetrized AGS operator that satisfies the equation

$$U(z) = PG_0(z)^{-1} + Pt(z)G_0(z)U(z), \qquad (21)$$

where $P = P_{231} + P_{312}$, P_{231} and P_{312} are the two cyclic permutations, and the energy $z = E - \frac{4}{3}k^2 + io$. Therefore the calculation of the $d + d$ elastic amplitude given by Eq. (20) implies the fully off-shell solution of Eq. (21) at a number of energy points running $\infty < z < E$.

Given the nature of the approximation we have developed, inelasticity in $d + d$ elastic scattering may be associated exclusively with processes such as dd $\to$ n^{3}He, dd $\to$ p^{3}H as well as dd $\to$ npd and dd $\to$ nnpp.

VII. EVALUATION OF THEORY

Despite the approximations we have undertaken, the calculations are still very challenging given the number of partial waves that are required for convergence at these energies. Therefore we limit ourselves to total four-body angular momentum $\mathcal{J}^\pm \leqslant 20^\pm$ and relative orbital angular momentum between the two deuterons $\mathcal{L} \leqslant 18$. For the $N + N$ interaction we choose the CD Bonn potential in partial waves $^1S_0, ^3S_1 - ^3D_1, ^1P_1, ^3P_0, ^3P_1$ and $^3P_2$ alone, and solve the corresponding AGS three-body equation for $N + d$ scattering with total three-body angular momentum $J^\pm \leqslant \frac{9}{2}^\pm$ and no restriction on the relative $N + d$ orbital angular momentum L.

Because the quality of this approximation for $d + d$ elastic scattering depends ultimately on the 2N and 3N input, we first discuss the implications of the approximation we make on 2N and 3N partial waves on $N + d$ elastic scattering. The number of 2N and 3N partial waves that are included is considerably smaller than what is required to get a fully converged 3N calculation at comparable energies. Nevertheless, because 3N forces are important at high energies, giving rise to an increase of the $N + d$ differential cross section minimum around $\theta_{c.m.} = 120°$, we show in Fig. 26 the results of a three-body calculation for the $N + d$ differential cross section at $E_d = 280$ MeV. The solid and the dashed lines respectively correspond to fully converged calculations with CD Bonn [33] and its coupled-channel extension CD Bonn+Δ [34] allowing for a single virtual Δ-isobar excitation and fitted to the experimental data
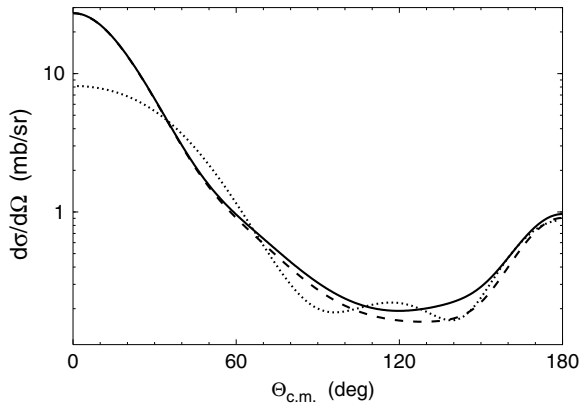
FIG. 26. Differential cross section for deuteron-neutron elastic scattering at $E_d = 280$ MeV. The solid and dashed lines correspond to fully converged calculations using CD Bonn $+ \Delta$ and CD Bonn, respectively; the dotted line corresponds to the actual $n + d$ t-matrix we use to calculate the $d + d$ amplitude.

with the same degree of accuracy as CD Bonn itself; the dotted line corresponds to a CD Bonn calculation where the number of 2N and 3N channels are limited to the ones mentioned above. Therefore the lack of convergence in terms of number of 2N and 3N partial waves overcompensates for the missing 3N force around $\theta_{c.m.} = 120°$ but is too low almost everywhere in the angular region. As a result of this limitation in the number of partial waves included in the calculation, the total $N + d$ elastic cross section is about 30% smaller than the one we get in the fully converged calculation with CD Bonn. Although at lower energies this limitation on the number of partial waves is less important than at higher energies, we expect this approximation to have a significant effect on the $d + d$ elastic cross section because, as mentioned before, the momentum integration in Eq. (20) implies the calculation of the $N + d$ off-shell amplitude for center of mass energies ranging from $E = E_{c.m.}$ to $E = -\infty$, where $E_{c.m.}$ is the four-nucleon center of mass energy.

We show the results of our calculation for the deuteron analyzing powers iT_{11}, T_{20}, and T_{22} in Figs. 18–20 as well as the differential cross section in Fig. 24. The solid curves correspond to calculations with the CD Bonn potential. As expected the $d + d$ differential cross section is well below the data, but the analyzing powers display some of features of the data: iT_{11} shows a broad peak at forward angles, while T_{22} decreases from zero up to $\theta_{c.m.} = 40°$ but does not follow the data points beyond $\theta_{c.m.} = 60°$. As for T_{20} the calculation only follows the data up to $\theta_{c.m.} = 30°$, after which it develops a minimum at $\theta_{c.m.} = 60°$ that is not supported by the data. We note that, except for the spin independence of the Coulomb interaction, there is no symmetry argument requiring T_{20} to be small at forward angles. Given the limitations of the $N + d$ input, illustrated by Fig. 26, we conclude that the proposed solution of the AGS equations gives a qualitative understanding of the data, particularly in the forward direction. Improvements are being considered with access to faster computers.

At this point we can only consider a range of possibilities for the $^3P_0$ partial wave associated with charge symmetry breaking pion production in the $d + d \rightarrow {}^4$He $+ \pi^0$ reaction. Because the lower $N + d$ partial waves that would most affect the $^3P_0$ wave are present, it may be relatively unaffected by the difficulties illustrated in Fig. 26. On the other hand, if we were to correct the shortfall in the cross section by increasing the contribution from all partial waves, we would not achieve agreement until the amplitudes are increased by as much as 50%. For now, we can take this range as an estimate of the uncertainty in the comparison of theory with experiment.

VIII. CONCLUSIONS

We reported here a set of angular distribution measurements of the cross section and three analyzing powers for $d + d$ elastic scattering at 231.8 MeV, an energy chosen to match the measurements of the charge symmetry breaking $d + d \rightarrow {}^4$He $+ \pi^0$ reaction. The hope was that these new data would provide a check of the four-body calculations used to describe the entrance channel in the theoretical treatment of the CSB reaction. These measurements were carried out with the broad range PINTEX detectors available on the Cooler ring at the end of the CSB experiment.

This was the first use of the PINTEX detectors for any observation based on the $d + d$ four-nucleon system. The presence of a large flux of three- and four-body final states and the limitations on energy resolution and kinematic information from the detectors made separation of both the $d + d$ and $d + p$ elastic scattering channels difficult. Especially for $d + d$ elastic scattering, the application of all available information did not result in a clear and unambiguous separation of this channel. As a result, the cross section in particular suffered from large systematic errors that grew out of these ambiguities.

The theoretical treatment of $d + d$ elastic scattering has also taken us into new territory. The solution of the AGS equations has required that we develop an expansion based on the lowest order terms in the Neumann series. The implementation of this approach still involves a very large space of angular momenta and producing a calculation required that this space be truncated. The effects of this severe restriction on just the three-nucleon scattering observables illustrates that there are still problems with the input to the four-body part of the calculation apart from the approximations made there.

It is difficult to judge the quality of the partial wave information that can be generated for use in the theoretical calculation of the CSB reaction. This is now a combination of the nature of the approximations used in the theoretical approach as well as the large systematic uncertainties associated with the experiment. Clearly improvements are needed on both sides. It is also important for many experiments that the ambiguity that presently exists with regard to the normalization of the $d + p$ cross section be resolved. Nevertheless, the general agreement between the calculations and the experiment, especially for the analyzing powers at forward angles, is promising. More experiments and continued work with the theory are needed to bring these studies of the four-nucleon system to maturity.

ACKNOWLEDGMENTS

[1] E. J. Stephenson *et al.*, Phys. Rev. Lett. **91**, 142302 (2003).

[2] A. Gårdestig, C. J. Horowitz, A. Nogga, A. C. Fonseca, C. Hanhart, G. A. Miller, J. A. Niskanen, and U. van Kolck, Phys. Rev. C **69**, 044606 (2004).

[3] A. Nogga, A. C. Fonseca, A Gårdestig, C. Hanhart, C. J. Horowitz, G. A. Miller, J. A. Niskanen, and U. van Kolck, Phys. Lett. **B639**, 465 (2006).

[4] U. van Kolck, J. A. Niskanen, and G. A. Miller, Phys. Lett. **B493**, 65 (2000).

[5] G. A. Miller, B. M. K. Nefkens, and I. Šlaus, Phys. Rep. **194**, 1 (1990).

[6] Gerald A. Miller, Allena K. Opper, and Edward J. Stephenson, Annu. Rev. Nucl. Part. Sci. **56**, 253 (2006).

[7] C. Alderliesten, A. Djaloeis, J. Bojowald, C. Mayer-Böricke, G. Paić, and T. Sawada, Phys. Rev. C **18**, 2001 (1978).

[8] V. Bechtold, L. Friedrich, M. S. Abdel-Wahab, J. Bialy, M. Junge, and F. K. Schmidt, Nucl. Phys. **A288**, 189 (1977).

[9] M. Garçon *et al.*, Nucl. Phys. **A458**, 287 (1986).

[10] E. O. Alt, P. Grassberger, and W. Sandhas, Phys. Rev. C **1**, 85 (1970); JINR No. E4-6688 (1972).

[11] R. E. Pollock, Annu. Rev. Nucl. Part. Sci. **41**, 357 (1991).

[12] http://www.iucf.indiana.edu/Experiments/PINTEX/pintex.html.

[13] T. Rinckel *et al.*, Nucl. Instrum. Methods A **439**, 117 (2000).

[14] V. P. Derenchuk and A. S. Belov, AIP Conf. Proc. **675**, 887 (2003).

[15] W. Haeberli, Annu. Rev. Nucl. Sci. **17**, 373 (1967).

[16] H. Gruebler *et al.*, Nucl. Phys. **A176**, 631 (1971).

[17] Harvey W. Clark, Ph.D. thesis, Ohio State University, 1981.

[18] M. Bittcher *et al.*, Few-Body Syst. **9**, 165 (1990).

[19] K. Sekiguchi *et al.*, Phys. Rev. C **65**, 034003 (2002).

[20] E. J. Stephenson, H. Witała, W. Glöckle, H. Kamada, and A. Nogga, Phys. Rev. C **60**, 061001(R) (1999).

[21] K. Ermisch *et al.*, Phys. Rev. C **71**, 064004 (2005).

[22] H. Postma and R. Wilson, Phys. Rev. **121**, 1229 (1961).

[23] G. Igo, J. C. Fong, S. L. Verbeck, M. Goitein, D. L. Hendrie, J. C. Carroll, B. McDonald, A. Stetz, and M. C. Makino, Nucl. Phys. **A195**, 33 (1972).

[24] K. Kuroda, A. Michalowicz, and M. Poulet, Nucl. Phys. **88**, 33 (1966).

[25] H. Rohdjeß *et al.*, Phys. Rev. C **57**, 2111 (1998).

[26] R. E. Adelberger and C. N. Brown, Phys. Rev. D **5**, 2139 (1972).

[27] K. Sekiguchi *et al.*, Phys. Rev. Lett. **95**, 162301 (2005).

[28] F. Ciesielski, J. Carbonell, and C. Gignoux, Phys. Lett. **B447**, 199 (1999).

[29] A. C. Fonseca, Phys. Rev. Lett. **83**, 4021 (1999).

[30] M. Viviani, A. Kievsky, S. Rosati, E. A. George, and L. D. Knutson, Phys. Rev. Lett. **86**, 3739 (2001).

[31] R. Lazauskas, J. Carbonell, A. C. Fonseca, M. Viviani, A. Kievsky, and S. Rosati, Phys. Rev. C **71**, 034004 (2005).

[32] O. A. Yakubovsky, Yad. Fiz. **5**, 1312 (1967) [Sov. Nucl. Phys. **5**, 937 (1967)].

[33] R. Machleidt, Phys. Rev. C **63**, 024001 (2001).

[34] A. Deltuva, R. Machleidt, and P. U. Sauer, Phys. Rev. C **68**, 024005 (2003).